Contents

CHAPTER 14

Interaction Region and Detector Interface

Contents

14.1 Introduction

In this chapter we examine various aspects of experimentation that directly interacts with the accelerator design. Of particular concern in this area is the background to the physics experiments that are caused by the beams passing through the detector.

The characteristics of background events at JLC will be very different from those at typical e^+e^- colliders, except the SLC. The features of the background strongly depend on numerous operational parameters of the accelerator, such as the beam aspect ratio (typically $\sigma_x^*/\sigma_y^* = 0(100)$), a high beam intensity (10^{10}particles/bunch) and possible tails in the particle distribution that deviates from a Gaussian distribution. The population of low energy $e^\pm$ pairs that are created during collisions are directly related to the beam aspect ratio, while the tail is mostly responsible for synchrotron radiation and muon background. The optimization of the machine operational parameters must be considered by taking this "interaction" between the experimentation and the machine into account. The highest-priority goal here is, of course, to maximize the luminosity while minimizing the background. With such a motivation in mind, the effects of $e^\pm$ pairs have been estimated by detailed Monte Carlo simulations with the proposed JLC-1 detector[1], in addition to simulations of masking of synchrotron radiation and the attenuation of the muon flux that are produced by interactions of the beams with upstream collimator materials.

Another important issue is the need for measurements of the distribution of the center-of-mass energy within each beam collision, hereafter called the "luminosity spectrum." At TeV linear colliders, particles in the colliding beams loose a significant amount of energy before "collisions" take place. This is due to the emission of synchrotron radiation in a strong electromagnetic field produced by the opposite beam, known as the "beamstrahlung" phenomenon. Therefore, the effective luminosity at $\sqrt{s} = 2 \times E_{beam}$ is always smaller than the nominal value that does not take beamstrahlung into account. The luminosity spectrum as a function of the center-of-mass energy depends on the magnitude of beamstrahlung. Knowledge on such issues is very important for conducting precision measurements, especially for studies of toponium physics[2] and detailed investigations of SUSY physics[3], which are research opportunities unique to linear colliders. A method based on the measurement of acollinearity angles in Bhabha scattering events is examined as a possible technique to measure the luminosity spectrum.

Detailed engineering design studies for the interaction region are not ready at this moment, and, thus, they will not be given in this chapter. No consideration of the support system of the final focus quadrupole magnets and the heavy masking system are given. The designs of the extraction beam lines and measurements of electron polarizations are not discussed, either. These issues are left for subsequent design studies in the near future.

14.2 Background

To illustrate where the background particles can originate, the beam line from the exit of the main linear accelerator (linac) to the interaction point (IP) is schematically shown in Figure 14.1. A +7 mrad bending magnet section (200 m long) downstream of the collimation section is needed in order to create a sufficient amount of separation for two experimental halls and to prevent the background from the upstream linac from directly hitting the detector. In the final focus system, beams are gradually deflected so as to have a horizontal beam crossing angle of ±4 mrad at the interaction point (IP).

There are two major sections for beam collimation (1200 m long) and a final focus system (1800m long) in the beam line to handle beam energies up to 0.75 TeV. While their main purposes are to clip the beam tails, secondary particles are inevitably produced, namely: (1) muons and (2) synchrotron radiation photons, respectively. In addition at the IP, (3) e^+e^- pairs and (4) mini-jet are created through beam-beam interactions. They all cause background hits in the detector facility.

In subsequent sections the first three kinds of background are discussed together with a possible design of the interaction region.

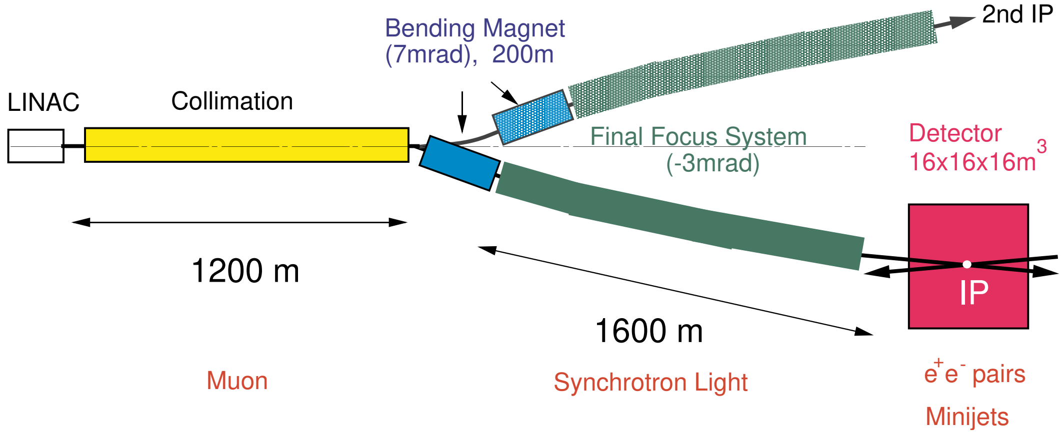

Figure 14.1: Top view of the beam line from the exit of the main linac to the interaction point (IP) at $E_{cm} = 0.5 - 1.5$ TeV.

14.2.1 Collimation and Muons

In this section we discuss the production of muons through the interaction of particles in the beam tails when they are collimated at the upstream collimation sections.

Generally, the transverse profile of the beam does not exactly follow a Gaussian distribution at linear colliders. The beams can be accompanied by long tails according to experience from experiments at SLC [4]. While the origin of these tails is not thoroughly understood at present, we shall conservatively assume that the beam has a flat tail beyond $\pm 3\sigma_{x(y)}$ in both the horizontal(x) and vertical(y) directions with a relative intensity of 1%.

As can be seen in the next section, the beam must be collimated within $\pm 6\sigma_x$ and $\pm 40\sigma_y$ in order to keep the background due to synchrotron radiation at a manageable level. Since the typical size of the beam core is on the order of a few μm, collimating such beams is a seriously non-trivial task. A work-around is to expand only the tail part sufficiently by using a non-linear collimation technique, as discussed in Chapter 13. This is part of the reason why a 1200 m-long collimator section is required for collimating a 0.75 TeV beam.

As stated in Chapter 2 and subsequent chapters, one RF pulse will accelerate a bunch train which contains up to 85 bunches separated by 1.4 nsec at a repetition rate of 150Hz. Since each bunch consists of 6.45×10^9 electrons (or positrons) at the IP, about 10^8(1%tail)$\times 10^2$(bunches) electrons may hit collimators at 150 Hz. In the interactions of the beam tails with the collimators a large number of muons are produced through the Bethe-Heitler process, $e^{\pm}N \rightarrow e^{\pm}\mu^+\mu^-N$. Without suitable measures these muons would traverse through the tunnel and create a large amount energy deposit within the detector facility. They would cause serious background problems for conducting high-energy physics experiments.

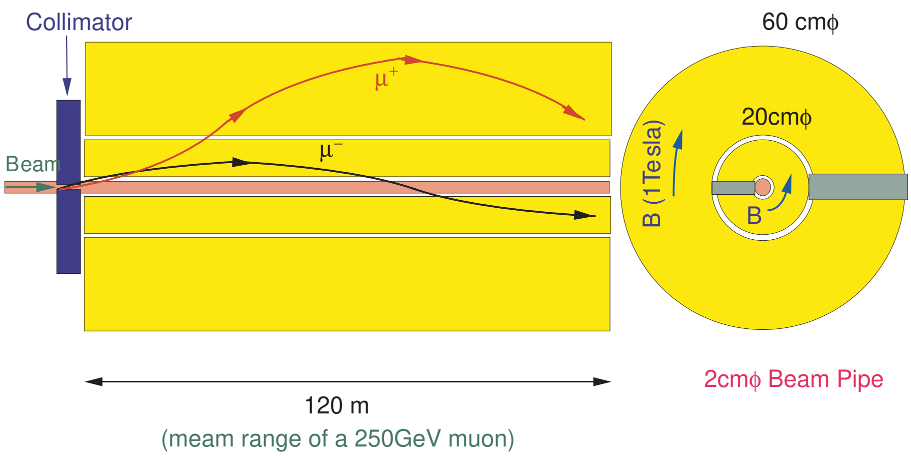

Figure 14.2: Original idea of a muon attenuator. Two iron pipes are magnetized axially in opposite directions for both charged muons, which can be trapped, where the 120m length of the iron pipe corresponds to a mean range of 250GeV muons.

Several techniques have been invented so far to reduce the muon background at linear colliders. The first is the "muon spoiler" idea, which was implemented at SLC. There, a set of large iron toroid magnets are installed in the beam line to over-focus the muons, so that they are dispersed away from the detector.

In the design study here, another method, which is called "muon attenuator", is considered. This idea was first proposed by by E.A.Kushnirenko [5]. The principle idea is to confine μ^+ and μ^- inside two iron pipes magnetized axially in opposite directions, and to absorb the muons by the energy loss.

A schematic diagram of this scheme is shown in Figure 14.2. We have performed a simulation study on the attenuation of muon flux onto the detector when this technique is applied. In the present JLC design there are six collimators in the collimation section between 1840 m and 2856 m, as measured from the IP. Various effects of long iron pipe shield of the attenuator was investigated with and without magnetization. The best condition was found to be the case with no magnetization in the iron pipes.

The outer and inner radius of the iron pipe shield are 31 and 1 cm, respectively. The beam pipe is located inside the iron pipes. The beam line between 1721 m to 2856 m from the IP except for the collimators is assumed to be covered with the iron shield. Muons that penetrate through the collimation section are bent by the big bend (+7 mrad, see Figure 14.1) and go through the tunnel of 3.5 mϕ. In this study a second bending magnet(-3.28 mrad) is assumed to be located at 80 m from the IP. This is so to make the horizontal beam crossing, although the actual design has several bending magnets distributed in the final focus system. Sand stone is assumed to surround the tunnel. The cross section of the tunnel is shown in Figure 4.78 of Ref.[1].

Figure 14.3 shows the result of the simulation. The horizontal axis gives the locations of collimators, as measured from the IP in meters. They correspond to the origins of muons. The vertical axis gives the number of electrons that are required to hit the collimators so that one muon produced out of these would to hit a detector of $16 \times 16 \times 16\text{m}^3$ volume size. The solid circle, solid triangle and open

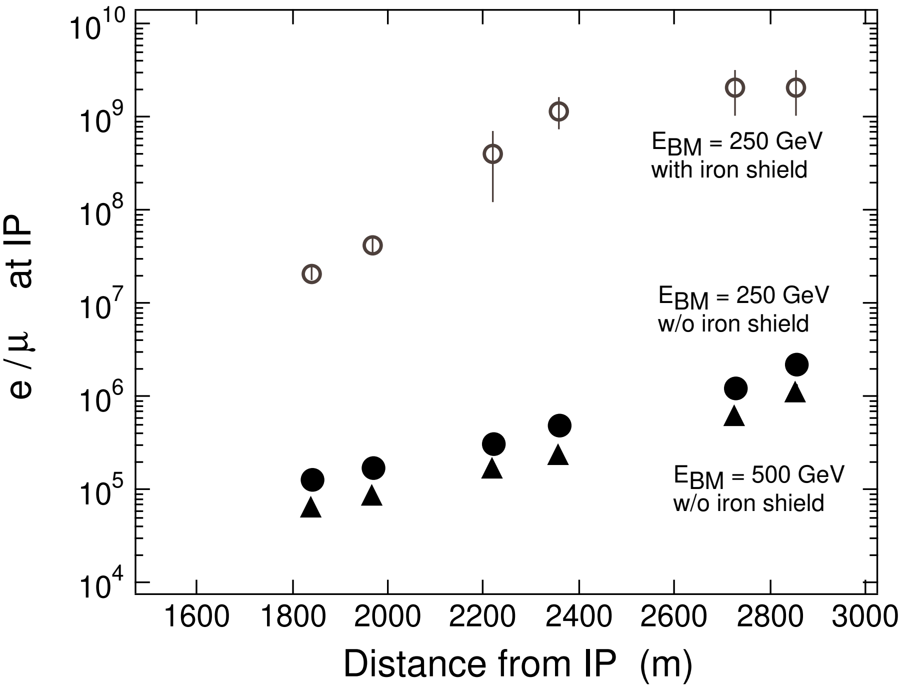

Figure 14.3: Number of electrons to produce one muon which reaches the IP.

circle symbols correspond to cases of the beam energies of 250 GeV without the iron shield, 500 GeV without the shield and 250 GeV with the shield, respectively. The result of the simulation can be summarized as below:

- The e/μ ratio is proportional to the inverse of the beam energy.
- The long iron pipe shield reduces the muon background by 2 or 3 orders of magnitude.

The "first" two collimators that are farthest from the IP are for momentum collimation, while the subsequent two sets would collimate elliptically the transverse beam profile ($6\sigma_x \times 40\sigma_y$) twice. A smearing effect, due to edge scattering off collimator jaws, has been calculated to be 10^{-4} beyond the edges of the ellipse by a single collimation. Consequently, from these results, we can estimate that at most 10 muons may traverse the detector at 150 Hz. Although this result seems to be acceptable for experiments, a further reduction of factor of 10 should be pursued for an additional safety margin. This additional reduction will be realized if muon spoilers are implemented in the final focus system, as studied in the NLC-ZDR[6].

14.2.2 Synchrotron Radiation

Since the intensity of synchrotron radiation is on the same order as the intensity of the beam, itself, it would be very harmful to the experimentation if they are scattered at the pole tips of the nearest quadrupole magnet QC1. It is also very difficult to shield them near to the IP. The amount of synchrotron radiation is determined by the maximum size and angular divergence of the beam profile. Both the maximum beam size (x, y) and the divergence (x', y') shall be well defined and controlled by the collimators.

The divergences can be expressed by $\sigma_{\theta_{x(y)}} = \sqrt{\epsilon_{x(y)}/\beta_{x(y)}}$, where $\beta_{x(y)}$ is a (optical) beta function in the final focus system and $\epsilon_{x(y)}$ is an emittance of beams. The beam size and the divergence are related by $\epsilon_{x(y)} = \sigma_{\theta_{x(y)}} \cdot \sigma_{x(y)}$. If we can not control them by some means, we must change the optics to enlarge $\beta_{x(y)}$ so that $\sigma_{\theta_{x(y)}}$ decreases. We may thus even have to sacrifice the luminosity because of $\sigma_{x(y)} = \sqrt{\epsilon_{x(y)} \cdot \beta_{x(y)}}$. A similar situation would likely occur at the beginning of operation with a larger emittance than the expected one, as happened in the SLC experiments.

Figure 14.4 shows the development of transverse beam envelops that correspond to $6\sigma_x \times 40\sigma_y$. Figure 14.4 covers the region from the IP up to the nearest dipole bend magnet. Here the smearing effect due to collimation is not taken into account, since it was estimated to be very small(10^{-8}) as mentioned earlier.

With a mask of 8 mmϕ radial aperture that is located at 30 m from the IP, synchrotron radiation from upstream magnets beyond the last bending magnet can be completely masked. Any synchrotron radiation that passes through the aperture of 8 mmϕ mask would pass through the final quadrupole magnet (QC1) without scattering. The half aperture of QC1 is chosen to be 6.85 mm. As can be clearly seen in Figure 14.4, the radiation from QC3 and QC2 provides the maximum divergence at the IP in the horizontal and vertical directions, respectively. The profiles of the radiation at the QC1 are shown in Figure 14.5. The length and inner aperture of QC1 are 2. 2m and 13.7 mmϕ, respectively. The front face of QC1 is located 2.0 m from the IP. The in-coming radiation passes through the central

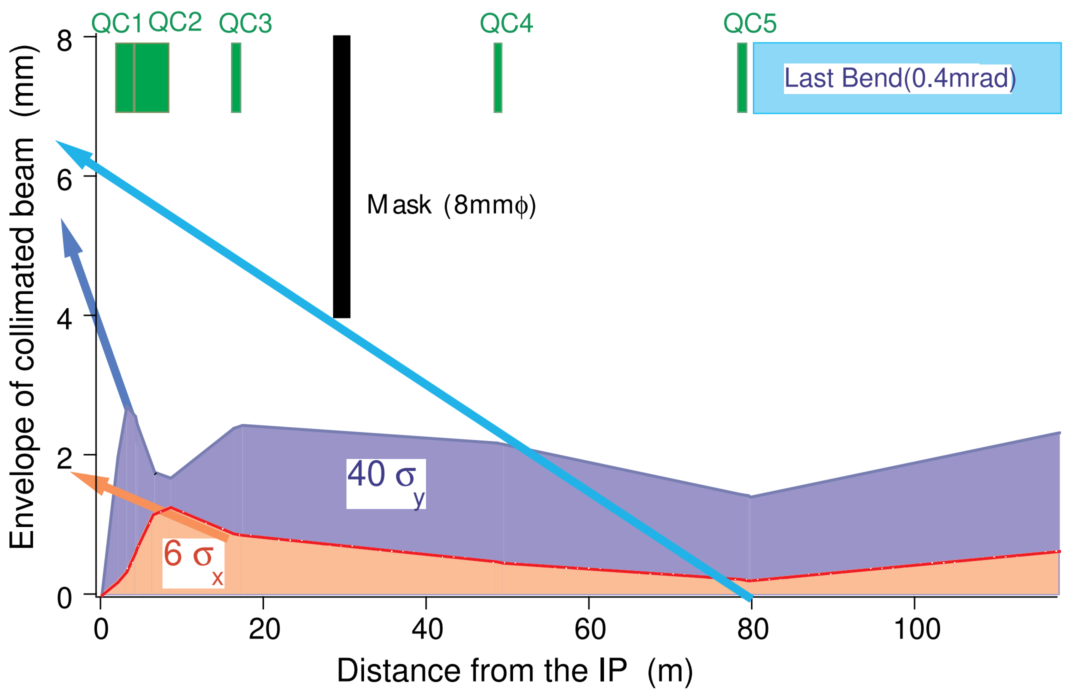

Figure 14.4: Horizontal($6\sigma_x$) and vertical($40\sigma_y$) beam envelopes through the last bending magnet and five final focus quadrupole magnets(QC1,QC2,QC3,QC4 and QC5). The maximum divergences of the synchrotron radiation are also drawn by arrows.

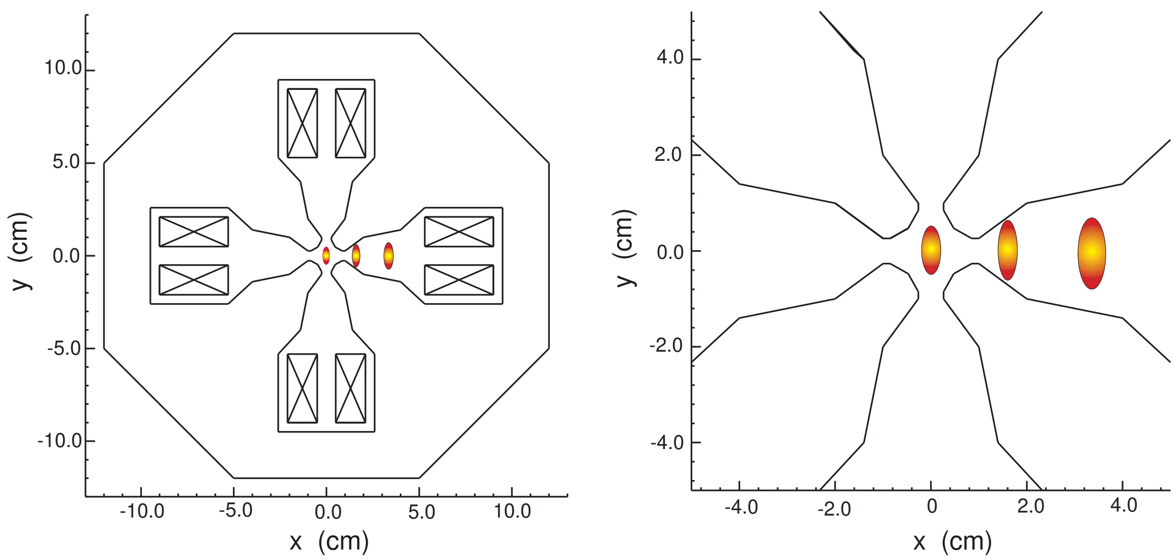

Figure 14.5: Profiles of the synchrotron radiation at QC1;right figure shows the magnified view around the center of QC1. The profile at the center accompanies the in-coming beam. The two right-hand side ones are passing through QC1 of 2.2m long after a collision with a 8mrad horizontal crossing.

axis of QC1. After colliding with the opposing beam at a horizontal crossing angle of 8 mrad, the out-going radiation passes off-axis through the QC1 magnet on the other side. The location of the out-going radiation is depicted as two elliptic profiles on the right-hand side of Figure 14.5.

As described above, it is expected that there should be no background problems due to the synchrotron radiation if we carefully optimize the collimation and the optics simultaneously.

14.2.3 e^+e^- pairs and Masking System

An enormous amount of e^+e^- pairs will be created during collisions, for instance a few times 10^5 pairs per bunch crossing. While their vast majority are scattered into extremely forward angles, some can be greatly deflected by the strong magnetic field that is produced by the on-coming beam. In such cases they can enter the detector region and can create background noise to the detector facility. Figure 14.6 shows the angular distributions of pair-produced electrons and positrons after the beam-

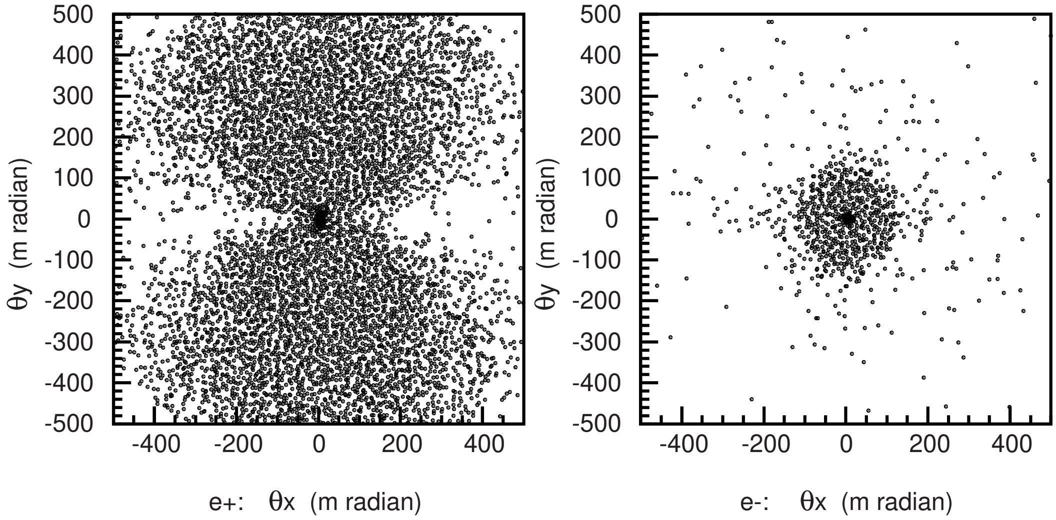

Figure 14.6: Electrons and positrons scattered by beam-beam interaction at IP. The vertical and horizontal axes denote the scattering angles in the vertical and horizontal directions, respectively. The left- and right-hand figures show the distributions of the positrons and electrons, respectively, downstream of the electron beam. Since the positrons have the same sign charge as the in-coming (positron) beam, they are scattered by larger angles than the electrons.

beam interaction. The calculation was made using ABEL[7]. Many particles (electrons or positrons) are scattered at large angles exceeding 200 mrad. We can also clearly see an asymmetry in their azimuthal distribution. More particles are deflected in the vertical direction than in the horizontal because of a very flat transverse beam profile ($\sigma_x^*/\sigma_y^* = 260\text{nm}/3.0\text{nm}$). Since the energies of the particles are relatively small, and are at a few hundreds MeV, most of these particles are confined near to the beam axis due to the detector solenoid magnetic field of 2 T. However, when they hit QC1 in the out-going side, many secondary photons are back-scattered uniformly into the detector region.

They can become serious background.

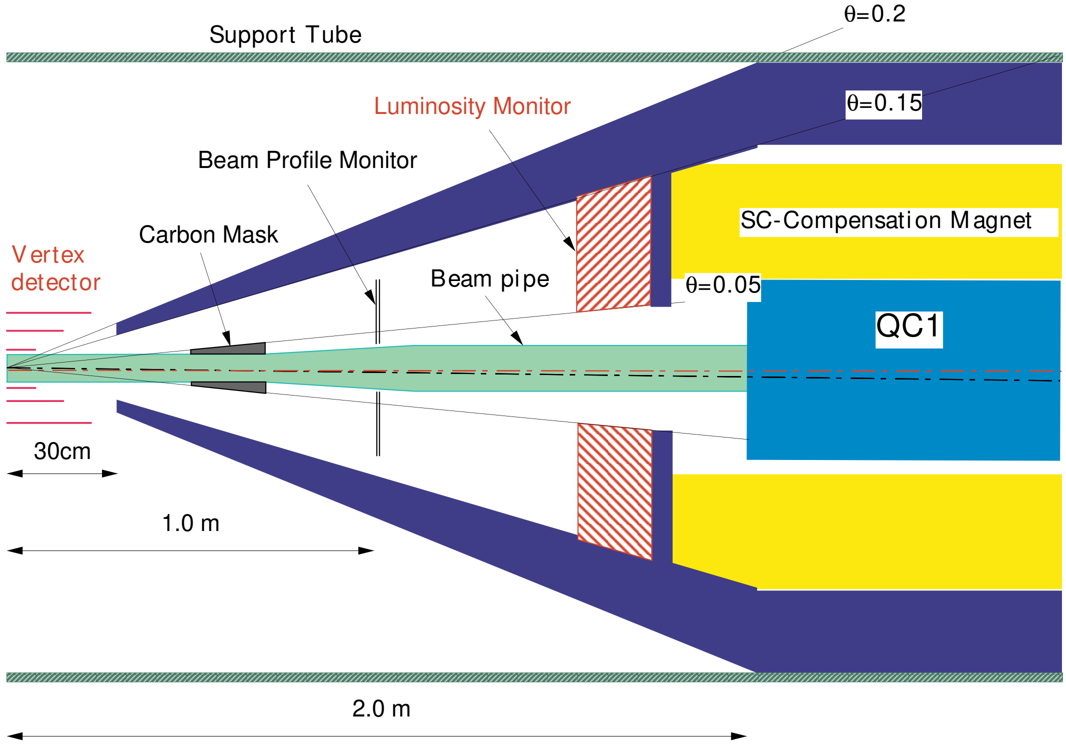

Figure 14.7: Schematic view of the interaction region for E_{cm} =0.5TeV.

A possible configuration of the interaction region is shown in Figure 14.7. A cone-shaped mask of heavy metal (tungsten) will be used to absorb the photons with good efficiency. The mask occupies a polar angle region of 0.15< θ <0.2 . The front aperture of the mask needs to be minimized in the light of reducing the background. However, it has to let the core part of the incoming beam pass through. An aperture size of r = 4.5 cm was chosen. The conical mask is mechanically connected to a 10.36 cm-thick cylindrical mask of the same material in a hermetic manner. A doublet of the final focus quadrupole magnets, QC1 and QC2, is implemented inside the mask. QC1 and QC2 are surrounded by a super-conducting solenoid magnet that compensates for the detector solenoid field of 2 T.

A detailed engineering design of the compensating magnet is not yet complete. However, naturally, a sufficient space needs to be allocated to accommodate these magnets inside the mask. In addition, inside the conical mask, two kinds of detectors will be installed: a beam profile monitor (at 1 m from the IP, to be described in the next section), and a luminosity monitor of tungsten-scintillator sandwich type (at 1.63 m from the IP, covering $0.05 < \theta < 0.15$). A set of 20 cm-thick carbon masks is also implemented (0.5 m from the IP). The carbon mask is designed to absorb back-scattered low energy particles. The mask will be built as an “active” device, which generates signals to veto scattered electrons/positrons at θ >0.05 in combination with with the luminosity monitor. They are considered to be important detector elements for studies of SUSY physics[3].

In order to estimate the background due to low-energy electron-positron pairs in the detector, numerical simulations have been conducted. The pairs, which are generated by the ABEL code, were tracked by employing a Monte Carlo program based on GEANT3.21[8]. This simulation software is called JIM (Jlc detector sIMulator). JIM takes account of the geometries of all the detectors, which have been described in the JLC-I[1], except for a few small revisions: The vertex detector is now assumed to have 3 layers instead of 2 as stated in JLC-I. The inner radius of the central drift chamber has been increased from 30 cm to 45 cm. Also the arrangement of the final focus quadrupole magnets(QC1 and QC2) and the masks follow the geometry shown in Figure 14.7.

For an accurate estimation of the background in the detectors, the threshold energies of the electrons/positrons and photons, *i.e.* the minimum energies to be tracked in JIM, have been set fairly low at 200 KeV and 10 KeV, respectively. The simulated statistics presented here corresponds to 10 bunch-crossings. The beam parameters used in this simulation were taken from the standard E_{cm} =500GeV operation. The values of the major parameters are: 6.45×10^9 e's/bunch, 85 bunches/train, a repetition rate of 150Hz, $\sigma_y/\sigma_x = 260/3$nm and a horizontal crossing angle of $\pm$4mrad. This corresponds to a luminosity of $8.1 \times 10^{33}\mathrm{cm}^{-2}\mathrm{s}^{-1}$ with a crab crossing. In this simulation the crab crossing was assumed to be perfect so that two beams collide head-on.

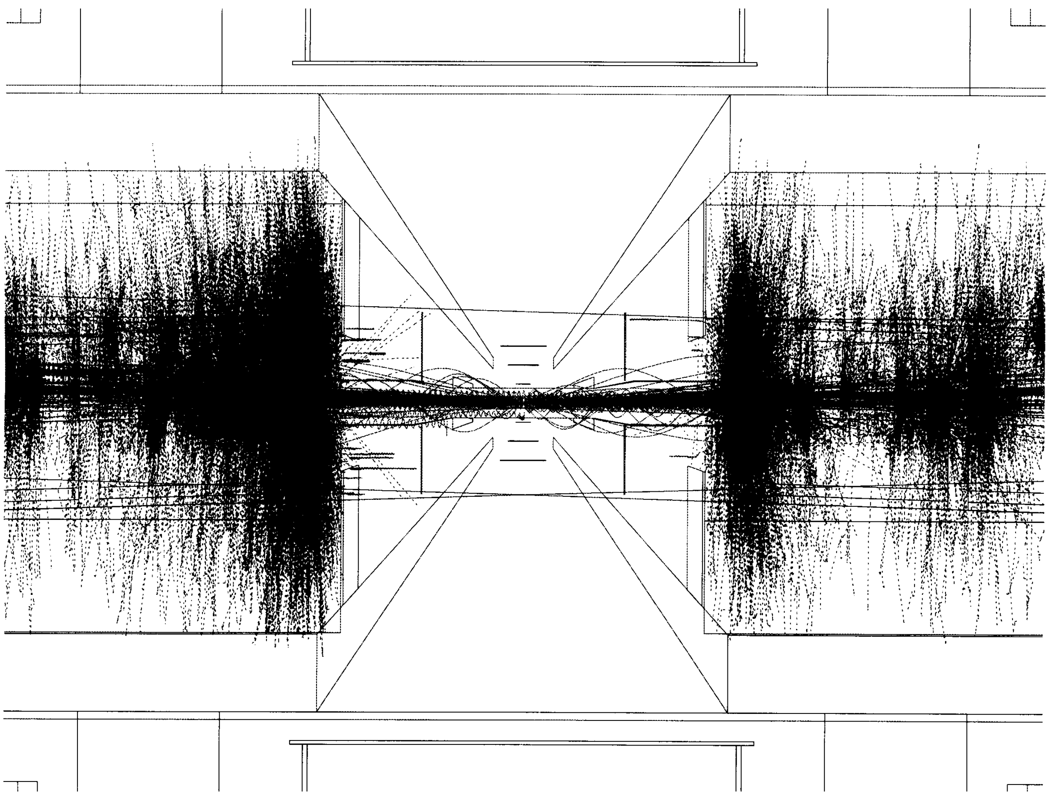

Figure 14.8: Particles of e^+e^- pairs simulated by JIM based on GEANT3, where the solid and dotted lines are electrons/positrons and photons, respectively. The statistics corresponds to 1/100 of a bunch crossing for a display purpose.

Figure 14.8 shows the pairs and secondary (back-scattered) particles simulated with the JIM code. As can be clearly seen in the figure, most of them, appearing like the core of dark band in the figure, pass through the front aperture (R_{mask}=4.5cm) of the mask. Particles outside of the core are scattered by much larger angles than the deflected ones, which represent a possible background to be considered.

The number of hits detected in the detectors is plotted as a function of the radial distance in Figure 14.9. The number of tracks that create those hits is similarly plotted in Figure 14.10. In these figures, the contributions from secondary particles are also plotted by solid circles. Here, the secondary particles are simply defined as those having off-vertex positions, *i.e.* $r_{vtx} > 0.5$mm or $z_{vtx} > 0.5$mm. We note here that the vertex detector consists of $25 \times 25\mu\text{m}^2$ pixels (CCDs), and that three layers

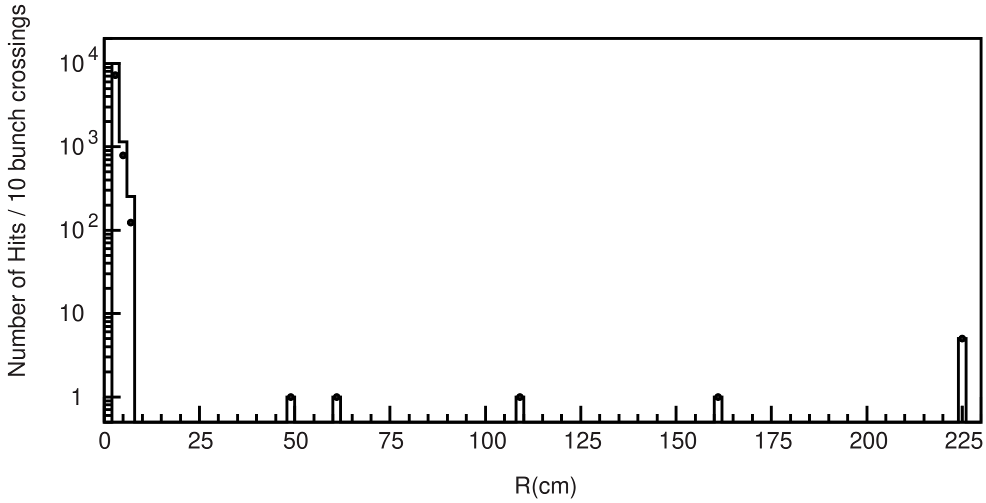

Figure 14.9: Number of hits detected in the detectors as a function of the radial distance for 10 bunch-crossings, where those produced by secondary particles are indicated by solid circles.

are located at r=2.5(z=±7.5 cm), 5.0(z=±15 cm) and 7.5cm(z=±22.5 cm). With these geometry parameters the hit densities were calculated to be 3.6, 0.1 and 0.01 hits/mm^2 for one machine pulse consisting of 85 bunch crossings (at 150Hz), respectively. We have assumed here that the hits are distributed uniformly within each layer. It should be noted, however, that since the actual angular distribution of pair particles is asymmetric, as shown in Figure 14.11, the hit counts quoted here represent only the average numbers.

On the average, a single charged particle track originating from the pair creation process will produce about 20 hits on the first layer of the vertex detector. This number is arrived at by comparing figures 14.9 and 14.10. Except for the first layer, the hit rates in the vertex detector are well below 1 hit/mm^2, which is considered an empirical limit[9, 6].

About a half of the hits in the first layer, as shown in Figure 14.9, are due to secondary particles. Contrary to our first expectation, the carbon mask was found to have no significant effect on the first layer background rate, while some reduction of hits was seen in the second layer. Figure14.12 shows transverse vertex positions (x, y for $z > 1.6$ m) of the secondary particles observed in the first layer.

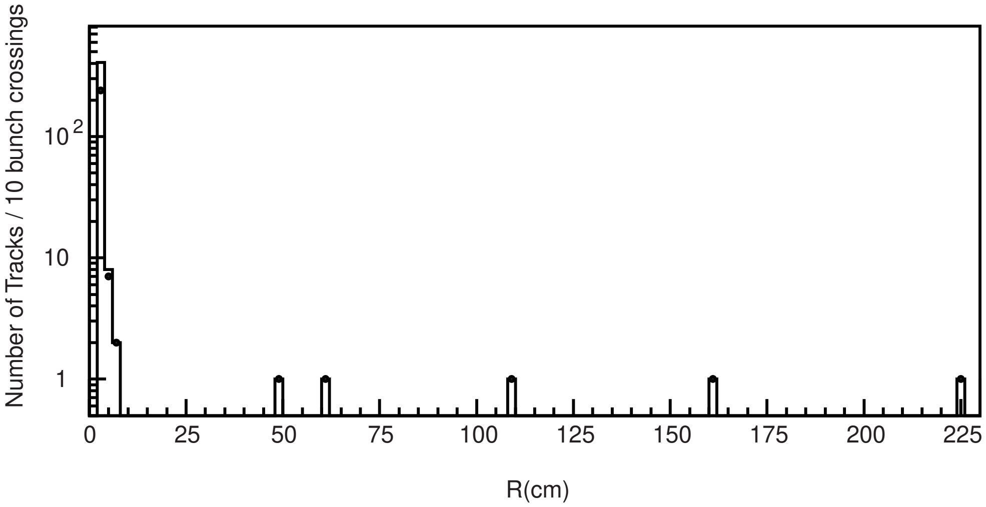

Figure 14.10: Number of tracks creating the hits in the previous figure as a function of the radial distance for 10 bunch-crossings, where those produced by secondary particles are also indicated by solid circles.

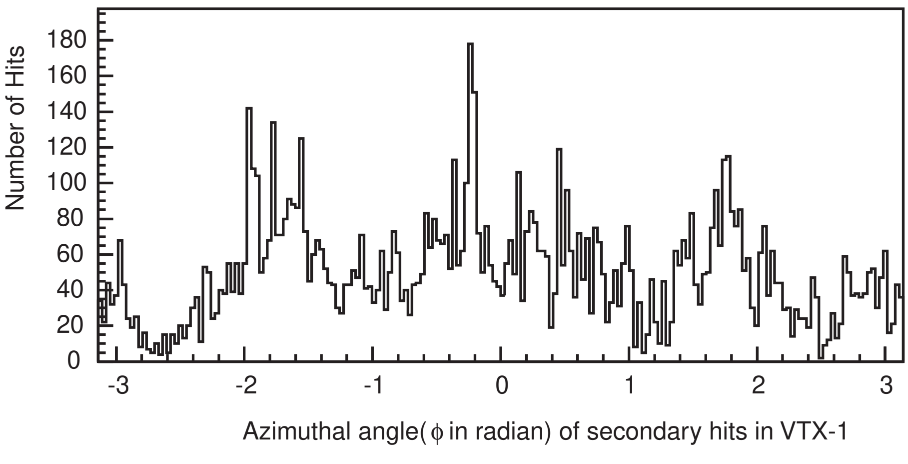

Figure 14.11: Angular distribution of hits on the first layer of the vertex detector for 10 bunch-crossings.

It should be recalled that this first layer can clearly see the pole tips of QC1. In fact, this may explain why the existence of the carbon mask did not quite help reduce the low-energy pair background on the first layer.

It is considered that more simulation studies and optimizations of the relative geometry of carbon masks are necessary. Also, a more detailed calculation of particle tracking with the vertex detector may reveal that for the first layer a background hit rate in excess of 1 hit/mm^2 is actually acceptable. This study should be also pursued.

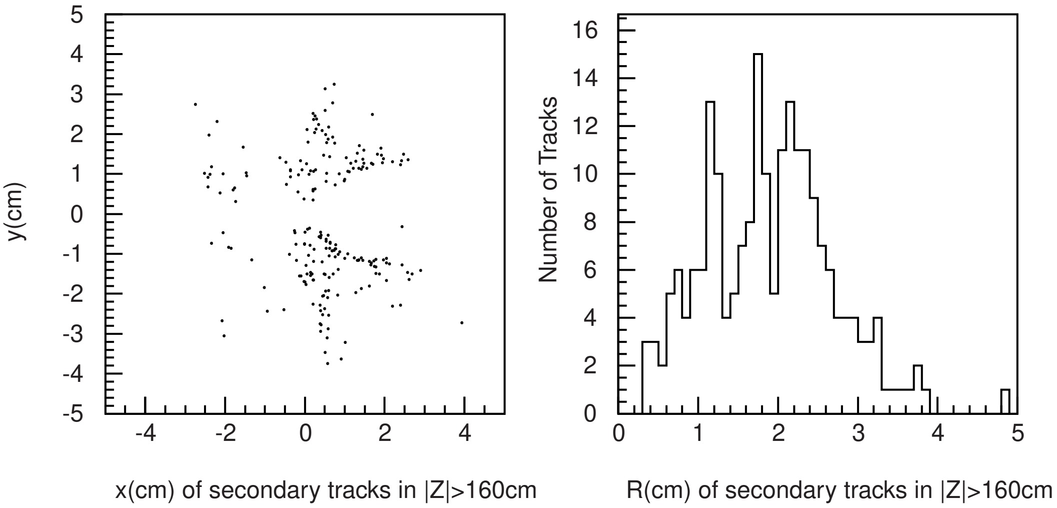

Figure 14.12: Transverse distribution of secondary particles at $z > 1.6m$ for 10 bunch-crossings.

In the central tracking region of $r > 45$cm, we expect about one hundred hits machine pulse (85 bunches per pulse at 150 Hz) as shown in Figure 14.9. This hit rate corresponds to ≈ 1 % occupancy in the tracking chamber. Since most of these hits are created by back-scattered photons, they are uniformly distributed in the tracking volume. Also their hit pattern is such that they rarely form contiguous hits that can be misidentified as charged particle tracks that originate from the IP. Therefore, no significant background problems from the pairs are expected in this region.

14.3 Beam Profile Monitor that Takes Advantage of $e^{\pm}$ pairs

As stated earlier, a large number of low-energy electron-positron pairs are produced through beam-beam collisions. Out of these low-energy particles, we hereafter call those that have the same charge as the oncoming beam "same-charge" particles. Particles with the opposite charge are called "opposite-charge" particles.

Figure 14.6 has shown that "same-charge" particles generally experience large deflections during the collision process because of the strong electromagnetic force due to the oncoming beam. On the other hand, the "opposite-charge" particles tend to oscillate inside the beam size space of the oncoming beam, because of the focusing force that is exerted on them. Consequently, the "opposite-charge" particles are scattered at much smaller angles.

This phenomenon is well described by a scattering process of $e^-(e^+)$ in a two-dimensional Coulomb potential which is Lorentz-boosted to the rest frame of the oncoming beam[10]. Since this potential is produced by the intense electric charge of the oncoming beam, it is a function of the transverse size (σ_x,σ_y) and intensity of that beam. Therefore, the distribution of deflected particles provides information on the oncoming beam, particularly its angular distribution. Hence, a measurement of the angular distribution of pair particles offers an excellent opportunity for determining the beam profile at the IP.

It should be noted that this technique allows one to measure the sizes of the two beams independently. This is because the low-energy particles are deflected asymmetrically in the forward and backward angular regions if the two beams have different beam parameters. It should be noted that there are two independent Coulomb potentials due to the two beams that are separated by a large relative Lorentz-boost along the beam axis. With a sufficiently accurate measurement of low-energy particle distributions, we can also measure the relative displacement and transverse rotation of two beams. In addition, this measurement can provide signals that can be used for a real-time, fast feedback to maintain the collision operation of the linear collider without disrupting the data collection by the experimental facility.

The basic characteristics and expected performance of this beam profile measurement technique has been extensively discussed in a published paper[11]. Here, we show some results from simulations with the JIM code.

We use the monitors that are located at ± 1 m (both sides) from the IP. They are arranged as shown in Figure 14.7. Each monitor consists of two layers of disk-shaped detectors. Each disk constitutes a pixel device which is made of 300μm-thick silicon. The monitor can measure both the radial position ($3 < r < 12$ cm) and the azimuthal angles ($-\pi < \phi < +\pi$) of the traversing particles with pixels of $50 \times 50 \mu\text{m}^2$ channel size. In addition, the pixel detectors will be arranged so that they can also measure the energy deposit left by the particles.

Figure 14.13 shows the simulated distributions of hits as measured by the two disks of the monitor at $z = 1$ m. Without taking specific measures to reduce the background, asymmetric angular distributions can be clearly seen over "uniform" backgrounds. The "maximum" radial distance can be found at around $r = 5.5$ cm.

Figure 14.14 shows the distribution of energy deposit on the beam profile monitor. The well-separated peak in this figure around 90 keV comprises the primary particles traversing the monitor, while peak around a lower energy deposit of 20 keV is created by the secondary particles which are backscattered from the QC1 and the luminosity monitor. It is seen that the energy deposits are very effective to discriminate the backgrounds. By selecting the hits associated with energy deposits > 70 keV,

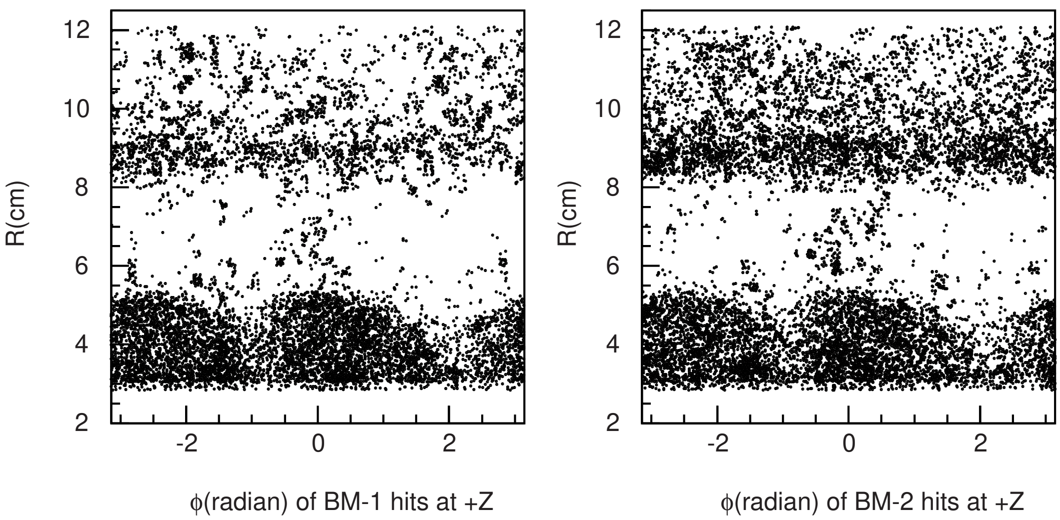

Figure 14.13: Hit distributions observed at two disks of the beam profile monitor at z=1m for 10 bunch-crossings. BM-2 is behind BM-1, as viewed from the IP.

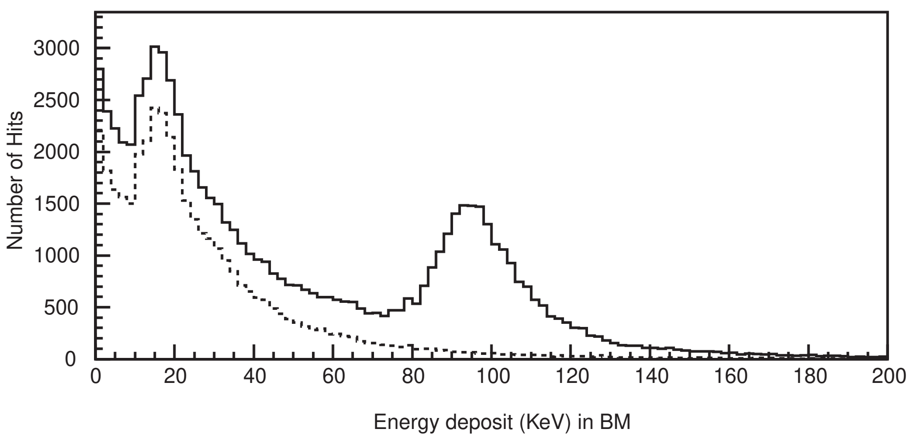

Figure 14.14: Energy deposits observed at the beam profile monitor for 10 bunch-crossings. The solid and dotted lines are for the total and secondary particles, respectively.

the signals of interest are significantly enhanced, as shown in Figure 14.15. Figure 14.16 shows

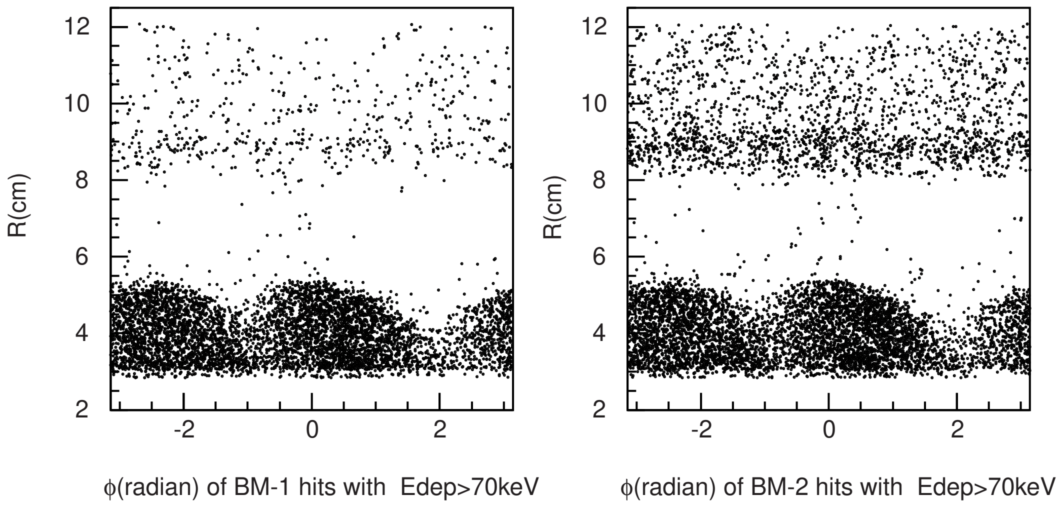

Figure 14.15: Distribution of hits whose energy deposit exceeds 70keV, as observed at the two disks of the beam profile monitor at $z = 1$ m for 10 bunch-crossings.

the hit angular distributions in the region $4.5 < r < 5.5$ cm. The hit pattern in this region carries information that is sensitive to the aspect ratio of the transverse beam sizes. As can be clearly seen in these figures, the asymmetric angular distribution can be measured very well with a very small amount of background.

These results indicate that the beam profile monitor based on measurements of low energy pair particles is a very promising technique.

14.4 Luminosity Spectrum

In typical $e^{\pm}$ colliding experiments, the luminosity is measured by counting the number of small angle Bhabha scattering events. This is a technique used under the assumption that the collision energy is reasonably monochromatic, except for the effect of the initial state radiation.

However, this is no longer a valid assumption in high energy linear colliders, including JLC. This is because of the significant energy spread in collisions associated with beamstrahlung energy loss. Rather, the differential luminosity with respect to the effective center-of-mass energy (hereafter called "luminosity spectrum") needs to be measured. Miller et al. have proposed an idea for measuring the luminosity-spectrum by using the acollinearity angle of the large angle Bhabha events[12]. The energy difference between e^+- and e^- beams appears in the acollinearity angle of the Bhabha scattering. The potentiality of this idea has been studied by means of a luminosity-spectrum generator and a Bhabha

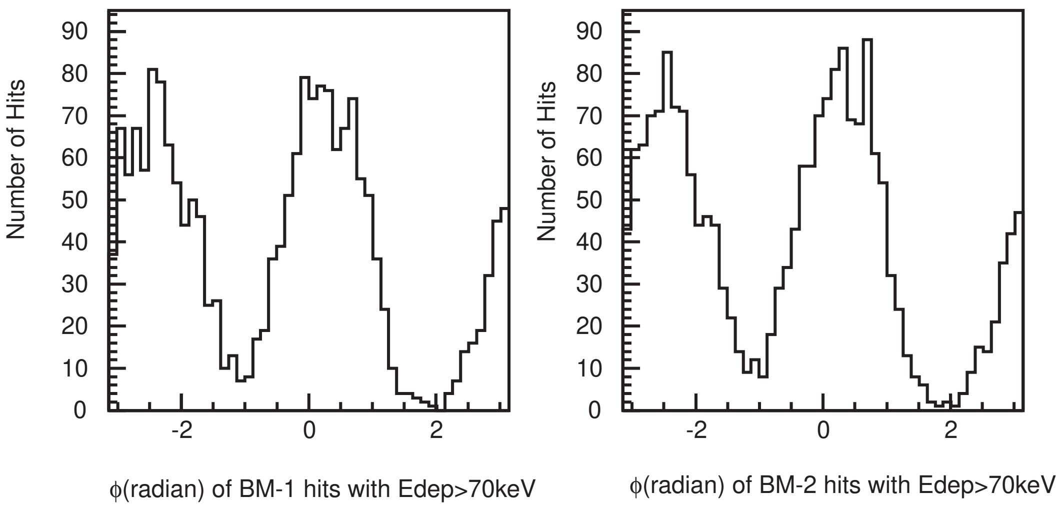

Figure 14.16: Angular distributions in $4.5 < r < 5.5cm$ for energy deposits of more than 70keV, observed at two disks of the beam profile monitor at z=1m for 10 bunch-crossings.

event-generator.

14.4.1 Event generation

In the past, an empirical formula used to describe the distribution of the collision energy at next-generation linear colliders has been presented by Yokoya and Chen[14]. In addition, recently developed software, called CAIN[13], is capable of simulating detailed beam-beam interactions at e^+e^-, $e\gamma$ and $\gamma\gamma$ linear colliders. The function in [14] has been found to give a good approximation to the CAIN calculation, as shown in Figure 14.17 at E_{beam}=250GeV. Table 14.1 summarizes the relevant parameters for the calculations.

Figure 14.17 shows that the function reasonably reproduce the CAIN result at $\sqrt{s} > 450$GeV, where a small difference seen in the figure is due to a beam disruption included in the CAIN.

To improve the efficiency of calculations, a luminosity-spectrum generator code has been created[15]. The generator code precisely reproduces the empirical function as shown in Figure 14.18.

It should be noted that besides the beam-beam interactions, the beam-energy spread also affects the luminosity-spectrum. Its effects were simulated, and the results are shown in Figure 14.19. In these calculations a uniform energy spread of $\pm 1\%$ was assumed for the original beams. It can be seen that the luminosity peaks are smeared at around $\sqrt{s}$=500GeV.

The differential cross section of the Bhabha scattering process was calculated using the program GRACE[16]. This is a program package for automatic amplitude calculations. The numerical integration and unweighted event generation were performed by two programs, BASES and SPRING[17], respectively. In this study, the lowest order Feynman diagrams of this process were taken into account,

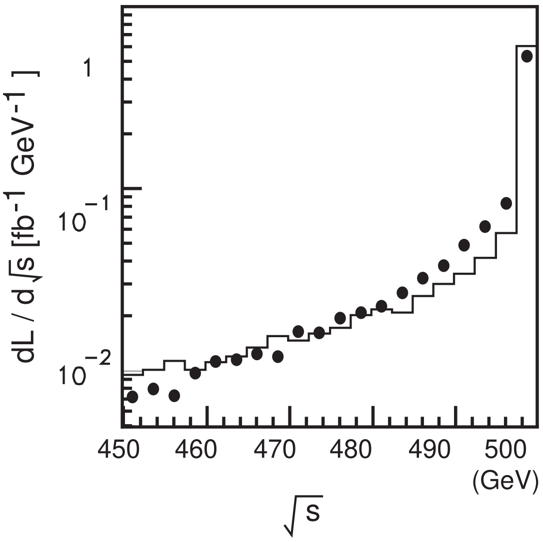

Figure 14.17: Luminosity spectra calculated by the empirical function (histogram) and CAIN (solid circles).

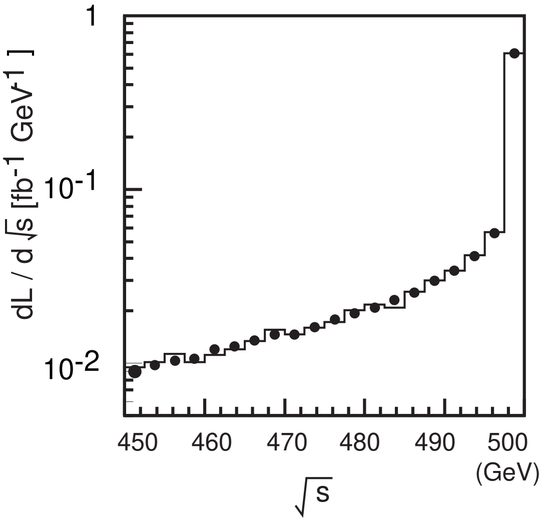

Figure 14.18: Luminosity spectra calculated by the generator (histogram) and the function (solid circles).

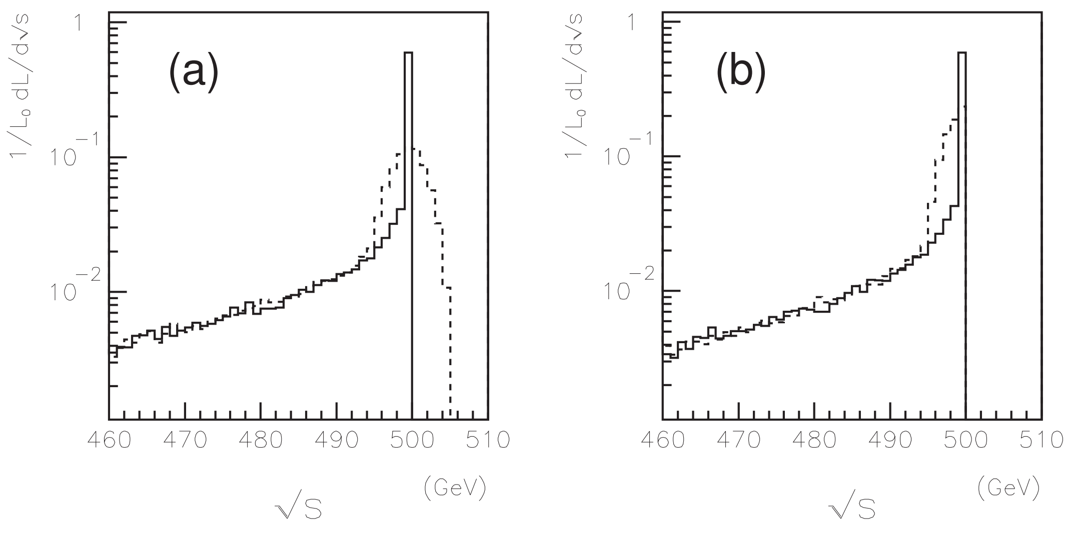

Figure 14.19: (a) The luminosity-spectra weighted by the Bhabha cross section, without (with) the ±1% uniform beam-energy spread, which is shown by the solid (dashed) histogram. (b) The spectra calculated by the acollinearity angles of the Bhabha events, where no entry above $\sqrt{s}$=500GeV exists by definition.

Item	value	unit
E_{beam}	250	GeV
f_{rep}	150	Hz
n_{bunch}	85	per pulse
$N_{particles}$	0.7×10^{10}	per bunch
ϵ_x	3.3×10^{-6}	m.rad
ϵ_y	0.048×10^{-6}	m.rad
β_x^*	10.0	mm
β_y^*	0.1	mm
σ_x^*	260.0	nm
σ_y^*	3.04	nm
σ_z	90	μm

Table 14.1: Major parameters of JLC.

since the effect of the initial state radiation can be precisely estimated[18].

14.4.2 Measurement of the Luminosity Spectrum

For Bhabha events, the momentum difference (ΔP) between e^+- and e^--beams can be expressed by

$$\Delta P = \frac{\theta_A P_b}{\sin \overline{\theta}}, \tag{14.1}$$

where θ_A is the acollinearity angle, P_b is the nominal beam momentum, and $\overline{\theta}$ is the average of e^+ and e^- polar angles.

Thus, the momentum difference can be calculated from the acollinearity angles of Bhabha events for the known nominal beam energy. The center-of-mass(CM) energy ($\sqrt{s_{meas.}}$) can be calculated using

$$\sqrt{s_{meas.}} = \sqrt{s_{nominal}} - \Delta P, \tag{14.2}$$

where $\sqrt{s_{nominal}}$ is the nominal CM energy, *i.e.* $2 \times E_{beam}$ for head-on collisions. Since θ_A is larger than zero, $\sqrt{s_{meas.}}$ must be less than (or equal to) $\sqrt{s_{nominal}}$. The beam-energy spread also produces events over the nominal beam-energy, as shown in Figure 14.19(a), while the $\sqrt{s_{meas.}}$ distribution is always below the nominal one as shown in Fig14.19(b). This is a limitation of this technique. In order to overcome this limitation for a sizable spread, we need additional information, such as the energies of scattered electrons and positrons.

Now, to separately examine the effects of the finite angular resolution of the detector, the beam energy spread is turned off. The measured spectrum with a perfect detector, *i.e.* with a perfect angular resolution, is compared with those with angular resolutions (σ_θ) of 3 mrad and 5 mrad in Figure 14.20. In a simulation the polar angles of both tracks are smeared by Gaussian distributions with the assumed angular resolution.

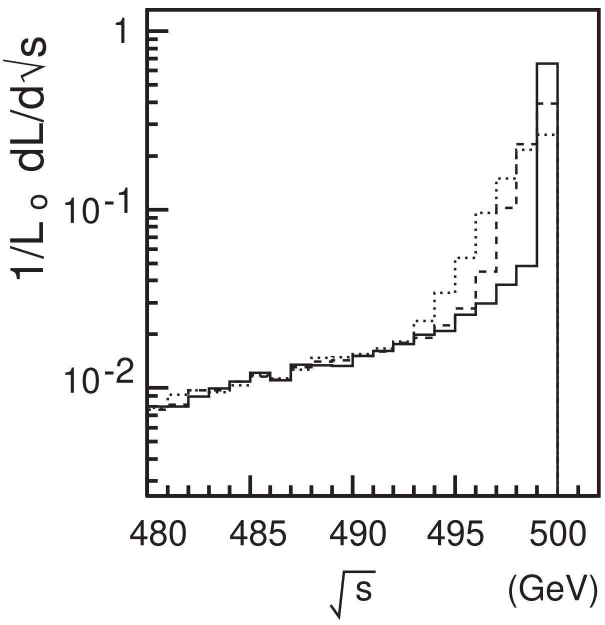

Figure 14.20: Luminosity-spectra as measured by the acollinearity angles of the Bhabha events. Various angular resolutions of measuring the Bhabha scattered particles are considered. Solid, dashed and dotted histograms correspond to angular resolutions of σ_θ=0(perfect), 3mrad and 5mrad, respectively.

The statistics of the simulation in Figure 14.19 corresponds to an accumulated luminosity of 10fb^{-1} (about one year accumulation). The detector is assumed to cover the polar angular region from 45° to 135°. Since the observed spectrum with $\sigma_\theta = 1$ mrad resolution is hardly distinguishable from the perfect detector case, it is not independently plotted in Figure 14.20. The spectrum with σ_θ >3 mrad shows a significant smearing effect.

For studies of toponium physics, accurate knowledge of the luminosity-spectrum within the total decay width of the top quark is very important. The top quark decay width is estimated to be 1.55GeV for m_{top} =175 GeV, *i.e.* ±0.5% of $\sqrt{s_{nominal}}$, according to the standard model. The performance of the accolinearity angle method in this narrow energy region needs to be examined. For this purpose, the integral luminosity for 455< $\sqrt{s}$ <450GeV to actually be obtained in collisions, and the luminosity values to be "measured" by this method are compared. Figure 14.21 shows the results of this study. The "nominal" (i.e. actual) luminosity is compared with the "measured" luminosity where various detector angular resolutions and polar angle coverages are assumed. It can be seen that an angular resolution better than 3 mrad is required for $\theta > 45°$ to maintain a satisfactory luminosity measurement performance. We also observed a slightly higher luminosity by 2.5% than the nominal one, even with the perfect resolution in Figure 14.21, since a small amount of luminosity must be added in a case that both beams can loose the same energies with no acollinearity angle, where $\sqrt{s_{meas.}} = \sqrt{s_{nominal}}$, by Equations 14.1 and 14.2.

When Bhabha-scattered particles within a smaller polar angle region are included in the analysis the

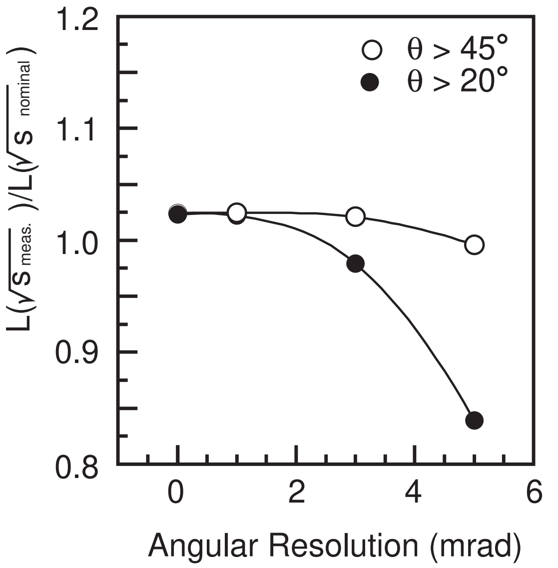

Figure 14.21: Luminosity normalized by the nominal one at $\sqrt{s} > 495GeV$ as a function of σ_θ in two angular regions of $\theta > 45°$(open circles) and $> 20°$(solid circles).

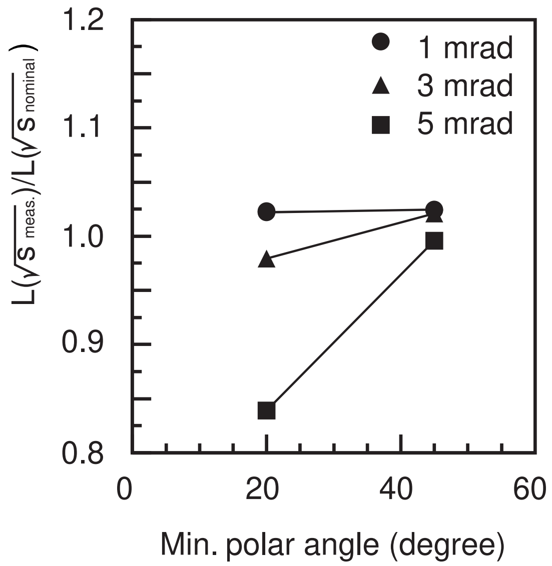

Figure 14.22: Luminosity normalized by the nominal one at $\sqrt{s} > 495GeV$ as a function of the minimum polar angle to be measured for various angular resolutions.

angular resolution of the measurement needs to be substantially improved because of a factor $1/\sin\overline{\theta}$ in Equation 14.1. On the other hand, the statistics of the Bhabha events increases very rapidly with decreasing the minimum polar angle (θ_{min}) to be measured. For example, the statistics for θ_{min}=20° increases by about one order of magnitude compared to that of θ_{min}=45°; therefore, the integrated luminosity can be reduced to 1fb^{-1} in the requirement. As shown in Figures 14.21 and 14.22, the angular resolution must be at least 1 mrad for θ_{min}=20°. The toponium experiment will involve an energy scan. It will consist of operations at several energy points each for a few fb^{-1}[2]. Therefore, it is essential to have σ_θ <1 mrad for θ >20°. The higher statistics is also favored in the light of reducing any possible systematic errors in the measurement of the luminosity.

14.4.3 Beam Parameter Fitting

Theoretically, the luminosity spectrum is determined by a set of beam parameters: the horizontal, vertical and longitudinal beam sizes $(\sigma_x, \sigma_y, \sigma_z)$ and the number of particles in a bunch(N). In the empirical function, two independent-valuables appeared as $B \equiv N/(\sigma_x + \sigma_y)$ and σ_z. They can be calculated from the measured spectrum, since the measured one is the luminosity spectrum convoluted by the cross section of the Bhabha scattering process, which is called the weighted luminosity spectrum. In this analysis, one of them is obtained by assuming a fixed value of the other, and vice versa, *i.e.* one parameter fitting in a likelihood method. The beam energy was set to be 250 GeV and the relevant parameters are listed in Table 14.1, which are called "nominal" beam parameters.

For this study, two kinds of Bhabha events were generated by the method described in the previous section. They are called an 'experimental-data sample' (e-sample) and a 'likelihood-function sample' (l-sample). The Monte Carlo statistics of e-samples corresponds to $10\mathrm{fb}^{-1}$ and $1\mathrm{fb}^{-1}$ for the angular regions of $\theta > 45°$ and $\theta > 20°$, respectively. The polar angles of electrons and positrons in the Bhabha events were smeared with a Gaussian distribution of 1mrad resolution; then, the weighted luminosity-spectrum was calculated as a function of $\sqrt{s}$ from their acollinearity angles. A number of e-samples were generated with several sets of B and σ_z. To determine a likelihood function, a l-sample was generated with 10 times more statistics than the e-samples with the nominal beam parameters. The weighted luminosity spectrum was obtained in the same way as the e-sample. Dividing the spectrum into 50 bins for 450< $\sqrt{s_{meas.}}$ <500GeV, the normalized likelihood function $\mathcal{L}$ was defined by

$$\mathcal{L}(I(\sqrt{s}); B, \sigma_z) \equiv N_l(I(\sqrt{s}))/N_{l-sample}, \tag{14.3}$$

where $I(\sqrt{s})$ is the bin-number corresponding to $\sqrt{s}$, $N_l(I(\sqrt{s}))$ is the number of events in the $I(\sqrt{s})$'th bin, and $N_{l-sample}$ is the total event number of the l-sample. For the e-sample, the log-likelihood was calculated by

$$\mathcal{LL} \equiv \sum_{j=1}^{N_{e-sample}} \ln \mathcal{L}_j, \tag{14.4}$$

where $N_{e-sample}$ is the total event number of the e-sample and $\mathcal{L}_j \equiv \mathcal{L}(I_j(\sqrt{s_j}); B, \sigma_z)$ is the likelihood of the j'th event in the e-sample.

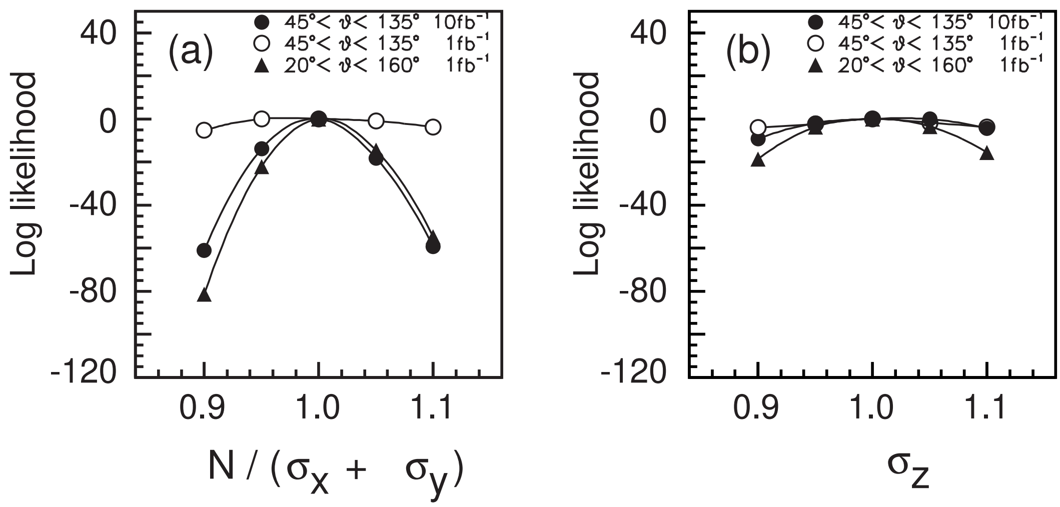

Figure 14.23: Log-likelihood distributions of the e-samples as a function of (a) $B = N/(\sigma_x + \sigma_y)$ and (b) σ_z, where the parameter was varied for ±10% relative to the nominal value, while the other was fixed to the nominal value and vice versa.

Figures 14.23(a) and (b) show the log-likelihood distributions as a function of B and σ_z, respectively. From these figures, it can be seen that the beam parameter of B or σ_z can be determined with an accuracy of several % by large ($\theta > 45°$) and small($\theta > 20°$) angle Bhabha events for an integrated luminosity of $10\mathrm{fb}^{-1}$ and $1\mathrm{fb}^{-1}$, respectively.

As described in the previous section, since the energy scan should be made for the integrated luminosity of a few fb^{-1} each at a number of CM energies around toponium resonance states[2], a 1 mrad angular resolution must be necessary in the small angular region ($\theta > 20°$). In these cases, the integrated luminosity of the peak in the luminosity spectrum must be precisely determined, although the peak may be smeared by the beam energy spread. It is seen that the present study has demonstrated the feasibility toward this end.

References for Chapter 14

[1] JLC-I, KEK Report 92-16, December, 1992.

[2] K.Fujii, T.Matsui and Y.Sumino,*Phys. Rev.* D **50**, 4341 (1994).

[3] M.M.Nojiri, K.Fujii and T.Tsukamoto, *Phys. Rev.* D **54**, 6756 (1996).

[4] D.Burke, proceedings of Workshop on *Physics and Experiments with Linear e^+e^- Colliders*, eds. R.Orava, P.Eerola and M.Nordberg (World Scientific, Singapore, 1992) p51, and references therein.

[5] E.A.Kushnirenko,proceedings of *The International Workshop on Final Focus and Interaction Regions of Next Generation Linear Colliders*, May 2-6,1992, *SLAC report* SLAC-405,p225.

[6] Zeroth-Order Design Report for the Next Linear Collider, LBNL-PUB-5424, also SLAC Report 474 or UCRL-ID-124161, May 1996.

[7] T.Tauchi, K.Yokoya and P.Chen, *Part. Accel.* **41**, 29 (1993).

[8] GEANT3.21-Detector Description and Simulation Tool, Application Software Group, computing and networks division, CERN, CERN Program Library Long Writeup W5013, March 1994.

[9] C.Damerell, private communication.

[10] K. Yokoya and P. Chen, "Beam-beam phenomena in linear colliders", lecture at 1990 US-CERN School on Particle Accelerators, Nov.7-14, 1990, Hilton Head Island, So. Carolina, USA, Lecture Notes in Physics 400. *Frontiers of Particle Beams: Intensity Limitations* , Springer Verlag, pp.415-445.

[11] T.Tauchi and K.Yokoya, *Phys. Rev.* E **51**, 6119 (1995).

[12] M.N. Frary, D.J. Miller, in: e^+e^- collisions at 500 GeV: the physics potential, ed.by P. Zerwas, DESY report 92-123A, 1992,p.379.

[13] P. Chen, G. Horton-Smith, T. Ohgaki, A.W. Weidemenn, K. Yokoya, Nucl. Instr. and Meth. **A355** (1995) 107.

[14] K. Yokoya, P. Chen, 'Electron energy spectrum and maximum disruption angle under multi-photon beamstrahlung', Presented at *the IEEE Particle Accelerator Conference, Chicago, 1989*, SLAC-PUB-4935 (1989).

[15] N. Toomi et al., in preparation.

[16] T. Ishikawa, T. Kaneko, K. Kato, S. Kawabata, Y. Shimizu, H. Tanaka. GRACE manual, KEK report 92-19, 1993

[17] S. Kawabata, Comp.Phys.Comm., **41** (1986) 127; *ibid.,* **88** (1995) 309.

[18] A. Arbuzov et al., Phys. Lett. **B383**(1996) 238.